POLARIZATION DEPENDENCY IN SEA SURFACE DOPPLER FREQUENCY AND ITS APPLICATION TO ENVISAT ASAR ALT-POL DATA

Ida Friestad Pedersen, Geir Engen, and Harald Johnsen

Norut Informasjonsteknologi AS, Box 6434, Forskningsparken, N-9294 Tromsø , Norway. e-mail: ida.friestad.pedersen@itek.norut.no

ABSTRACT

The capabilities of dual polarization SAR data to resolve or improve the wind/current retrieval based on Doppler measurements are investigated. The idea is that while the contribution from wind is polarization dependent, the contribution from a steady current is polarization independent. A theoretical framework for using Doppler information from SAR measurements for wind/current retrieval is developed and applied to Envisat ASAR Alternating Polarization Mode data. Theoretically computed Doppler frequency difference at C-band between HH and VV polarization as a function of wind speed and sea state for different incidence angles are presented. For a range wind of 7 m/s, values around 10 Hz is predicted for an incidence angle of 30°. Comparison with Doppler frequency estimates from Envisat Alt-Pol data show good agreement, both for the absolute Doppler frequency and the Doppler frequency difference.

1. INTRODUCTION

It has previously been shown that the Doppler frequency anomaly in Synthetic Aperture Radar data is highly correlated to the wind vector component along the radar line of sight [1], [2].

The anomaly arises because moving targets, such as the coherent backscattering elements riding on the ocean surface, produce Doppler shifts proportional to their relative velocities toward the receiving radar antenna. The motion of the ocean surface can be represented as a wave motion superimposed on a current $\mathbf{U}$. For coastal areas, this anomaly may then just as likely be connected to the coastal current component than to the wind, or a mixture between wind field and surface current.

In this paper, we investigate the capabilities of dual polarization SAR data to improve the wind retrieval based on sea surface Doppler frequency measurements. Of particular importance is to assess the performance of the VV-HH Doppler frequency difference.

The theoretical derivations are presented in section 2. We start by describing the SAR formalism, leading to an expression for the complex SAR image spectrum given in the end of section 2.1. This equation is the starting point for the rest of the derivations. The averaged product of two such complex SAR image spectra is considered in section 2.2, where the method of moments is used to estimate the Doppler shift of this spectrum due to the range direction motion of the imaged ocean surface.

In section 3, we describe the electromagnetic backscattering model source-function used in the computations, and use a statistical model for the ocean surface to find expressions for the Doppler frequency that easily can be numerically implemented. Section 4.1 shows the Doppler frequencies predicted by this formalism for different wind-speeds, angles of incidence and sea states. Comparisons with Doppler frequencies estimated from selected Envisat ASAR-scenes are presented in section 4.2.

2. THEORY

2.1. SAR-formalism

In ground-range coordinates $\mathbf{x}'$, the complex SAR raw-data image can be written as a convolution of the complex reflectivity of the imaged surface with the impulse response of the system [4]:

$$I_{\mathrm{raw}}(\mathbf{x}') = \int d\tilde{\mathbf{x}}\, e^{-i2\mathbf{k}_{\mathrm{h}}\cdot\tilde{\mathbf{x}}}\, \gamma(\tilde{\mathbf{x}}, t=\tfrac{y'}{v})\, f(\mathbf{x}'-\tilde{\mathbf{x}}; R). \tag{1}$$

Here $\mathbf{k}_{\mathrm{h}}$ is the horizontal projection of the radar wave vector $\mathbf{k}_{\mathrm{r}} = (\mathbf{k}_{\mathrm{h}}, k_{\mathrm{v}})$, γ is the complex backscatter coefficient, v is the radar platform velocity, R is the slant-range distance of the imaged object, t is the time and f is the signal spreading function:

$$f(\mathbf{x};R) = f_0(\mathbf{x};R)\,\tilde V(y)\,\tilde U(\tfrac{k_\mathrm{h}}{k_\mathrm{r}}x - \Delta R(y;R)) \quad (2)$$

$$f_0(\mathbf{x};R) = e^{-i2k_\mathrm{r}\Delta R(y;R) - i\frac{\alpha}{2}(\frac{k_\mathrm{h}}{k_\mathrm{r}}x - \Delta R(y;R))^2} . \quad (3)$$

In (2) and (3), $\tilde V$ is the radar azimuthal ground-pattern intensity function, $\tilde U$ is the envelope of the transmitted chirp signal, α is the signal chirp-rate and

$$\Delta R(y;R) = \sqrt{R^2+y^2} - R \approx \frac{y^2}{2R} \quad (4)$$

is the radar to target curvature function.

The complex backscatter coefficient at the ground range reference point $(\tilde{\mathbf{x}}, \tilde z = 0, t)$ for a time dependent dielectric surface can be written as

$$\gamma(\tilde{\mathbf{x}},t) = \int d\mathbf{x}''\,\delta(\mathbf{x}'' + \mathbf{k}_\mathrm{h}\tfrac{k_\mathrm{v}}{k_\mathrm{h}^2}\,\tilde\eta(\mathbf{x}'',t) - \tilde{\mathbf{x}})\,\tilde F(\mathbf{x}'',t) . \quad (5)$$

Here $(\mathbf{x}'', \eta(\mathbf{x}'',t), t)$ are the points on the surface with the same slant-range distance as the ground range point $(\tilde{\mathbf{x}},0,t)$, related by $\tilde{\mathbf{x}} = \mathbf{x}'' + \mathbf{k}_\mathrm{h}\,\tilde\eta(\mathbf{x}'',t)k_\mathrm{v}/k_\mathrm{h}^2$. Furthermore, $\tilde F$ is a source function caused by the electric surface current, generally non-linearly dependent on the surface elevation $\tilde\eta$. A model for $\tilde F$ was developed in [5] by use of the Stratton-Chu formalism [6], and will be further described later.

Inserting the expression for the complex backscatter coefficient into equation (1) then gives:

$$I_\mathrm{raw}(\mathbf{x}') = \int d\tilde{\mathbf{x}}\, e^{-2i\mathbf{k}_\mathrm{h}\cdot(\tilde{\mathbf{x}} + \mathbf{k}_\mathrm{h}\frac{k_\mathrm{v}}{k_\mathrm{h}^2}\tilde\eta(\tilde{\mathbf{x}},\frac{y'}{v}))}\,\tilde F(\tilde{\mathbf{x}},\tfrac{y'}{v})\; f(\mathbf{x}' - \tilde{\mathbf{x}} - \mathbf{k}_\mathrm{h}\tfrac{k_\mathrm{v}}{k_\mathrm{h}^2}\,\tilde\eta(\tilde{\mathbf{x}},\tfrac{y'}{v});R) . \quad (6)$$

In this work, we let the time-dependent surface be the air-sea interface. Assume now that the surface elevation function $\tilde\eta$ at position $\tilde{\mathbf{x}}$ can be written on the following form:

$$\tilde\eta(\tilde{\mathbf{x}},t) = \eta(\mathbf{x},t)$$

where $\mathbf{x}$ is the solution of

$$\tilde{\mathbf{x}} = \mathbf{x} + \boldsymbol{\xi}(\mathbf{x},t) ,$$

and the vector $\boldsymbol{\chi} = (\boldsymbol{\xi},\eta)$ represents the orbital motion of a fluid particle measured at the reference point $\mathbf{x}$. This formulation describes the motion by following the individual fluid particles, and is known as the Lagrangian description of fluid motion [8].

By changing to the reference system following the horizontal displacement $\boldsymbol{\xi}$ of the fluid-particles: $\tilde{\mathbf{x}} \to \mathbf{x} + \boldsymbol{\xi}$, eq.(6) can be written as

$$I_\mathrm{raw}(\mathbf{x}') = \int d\mathbf{x}\, e^{-2i\mathbf{k}_\mathrm{h}\cdot(\mathbf{x} + \boldsymbol{\chi}_\mathrm{p}(\mathbf{x},\frac{y'}{v}))}\,F(\mathbf{x},\tfrac{y'}{v})J(\mathbf{x},\tfrac{y'}{v})\; f(\mathbf{x}' - \mathbf{x} - \boldsymbol{\chi}_\mathrm{p}(\mathbf{x},\tfrac{y'}{v});R) , \quad (7)$$

where we have defined

$$\boldsymbol{\chi}_\mathrm{p} = \boldsymbol{\xi} + \mathbf{k}_\mathrm{h}\tfrac{k_\mathrm{v}}{k_\mathrm{h}^2}\,\eta , \quad J = \det\begin{bmatrix} 1+\frac{\partial\xi_\mathrm{x}}{\partial x} & \frac{\partial\xi_\mathrm{y}}{\partial x} \\ \frac{\partial\xi_\mathrm{x}}{\partial y} & 1+\frac{\partial\xi_\mathrm{y}}{\partial y}\end{bmatrix} ,$$

and

$$F(\mathbf{x},\tfrac{y'}{v}) = \tilde F(\mathbf{x}+\boldsymbol{\xi},\tfrac{y'}{v}) .$$

We now start by Fourier transforming $I_\mathrm{raw}(\mathbf{x}')$ in range and azimuth, to obtain the 2D-Fourier transformed raw-data image. By applying the method of stationary phase, which requires the derivatives of the phase term with respect to x and y to be zero, we find that the Fourier transformed image may be approximated by

$$\hat I_\mathrm{raw}(\mathbf{k}) \approx \int d\mathbf{x}\, e^{-i(2\mathbf{k}_\mathrm{h}+\mathbf{k})\cdot(\mathbf{x}+\boldsymbol{\chi}_\mathrm{p}(\mathbf{x},t_\mathrm{s}))}\,F(\mathbf{x},t_\mathrm{s})\; J(\mathbf{x},t_\mathrm{s})\,\hat f_0(\mathbf{k};R)\,\tilde U(x'_\mathrm{s})\,\tilde V(y_\mathrm{s}) . \quad (8)$$

Here $\hat f_0$ is the 2D-Fourier transform of f_0, x_s, y_s are the stationary phase values of x and y given by:

$$x_\mathrm{s} = \frac{k_\mathrm{r}}{k_\mathrm{h}}\Delta R - \frac{1}{\alpha}\frac{k_\mathrm{r}^2}{k_\mathrm{h}^2}k_\mathrm{x} , \quad (9)$$

$$k_\mathrm{y} + \left(2k_\mathrm{r} + \frac{k_\mathrm{r}}{k_\mathrm{h}}k_\mathrm{x}\right)\frac{y_\mathrm{s}}{R} + (2\mathbf{k}_\mathrm{h}+\mathbf{k})\cdot\dot{\boldsymbol{\chi}}_\mathrm{p}(\mathbf{x},t_\mathrm{s})\tfrac{1}{v} = 0 , \quad (10)$$

x'_s is given by $x'_\mathrm{s} = \frac{k_\mathrm{h}}{k_\mathrm{r}}x_\mathrm{s} - \Delta R = -\frac{1}{\alpha}\frac{k_\mathrm{r}}{k_\mathrm{h}}k_\mathrm{x}$, and t_s is given by $t_\mathrm{s} = (y + y_\mathrm{s} + \xi_\mathrm{y})/v$. Since ξ_y/v represents a small time offset (less than 10^{-3} s for satellite systems), the following approximation may be done:

$$t_\mathrm{s} \approx \frac{y+y_\mathrm{s}}{v} . \quad (11)$$

If we make a first order Taylor expansion of $\dot{\boldsymbol{\chi}}_\mathrm{p}$ with respect to t_s around y/v, and assume the system to be narrow-banded, $|\mathbf{k}| \ll k_\mathrm{h}$, we get the following stationary phase value:

$$y_\mathrm{s} \approx -\frac{k_\mathrm{y} + 2\mathbf{k}_\mathrm{h}\cdot\dot{\boldsymbol{\chi}}_\mathrm{p}\,\frac{1}{v}}{\frac{2k_\mathrm{r}}{R} + 2\mathbf{k}_\mathrm{h}\cdot\ddot{\boldsymbol{\chi}}_\mathrm{p}\,\frac{1}{v^2}} \approx -\frac{R}{2k_\mathrm{r}}k_\mathrm{y} - \frac{R}{k_\mathrm{r}v}\left(\mathbf{k}_\mathrm{h}\cdot\dot{\boldsymbol{\chi}}_\mathrm{p}\right) + \frac{R^2}{2k_\mathrm{r}^2v^2}\left(\mathbf{k}_\mathrm{h}\cdot\ddot{\boldsymbol{\chi}}_\mathrm{p}\right)k_\mathrm{y} . \quad (12)$$

It can be shown that in equation (12), the second term represents a shift of the profile $\tilde V$ due to the motion of the surface in range, while the last term represents a deformation of $\tilde V$. We will in the following concentrate on the shift of $\tilde V$, and therefore neglect the last term of eq. (12).

The SAR data-compression, producing the complex SAR image spectrum, is now done by removing the dependence of $\hat f_0$ (multiplying with $\hat f_0^{-1}$), yielding:

$$\hat I_\mathrm{c}(\mathbf{k}) \approx \int d\mathbf{x}\, e^{-i(2\mathbf{k}_\mathrm{h}+\mathbf{k})\cdot(\mathbf{x}+\boldsymbol{\chi}_\mathrm{p}(\mathbf{x},t_\mathrm{s}))}\,F(\mathbf{x},t_\mathrm{s})\; J(\mathbf{x},t_\mathrm{s})\,\tilde U(x'_\mathrm{s})\,\tilde V(y_\mathrm{s}) . \quad (13)$$

This equation is the basic starting point for describing the different aspects of SAR imaging.

2.2. Doppler frequency

Based on equation (12), we have stated that the range-direction motion of the surface will lead to an azimuthal shift of the complex SAR image spectrum. This is the Doppler frequency, and it can be estimated by considering the averaged product $\langle \hat{I}_{\rm c}(\mathbf{k})\hat{I}^*_{\rm c}(\mathbf{k})\rangle$ of two complex image spectra and applying the method of moments. Here, the superscript * denotes the complex conjugate value, and $\langle\rangle$ is the expectation operator. Assuming the backscatter to be constant for small variations in $\mathbf{k}$, we neglect the $\mathbf{k}$-dependence of $t_{\rm s}$ and the exponential in (13), and define

$$\mathcal{J}(\mathbf{x}) = J(\mathbf{x}, t_{\rm c})\;, \quad \mathcal{F}(\mathbf{x}) = F(\mathbf{x}, t_{\rm c})\;,$$
$$\zeta(\mathbf{x}) = 2\mathbf{k}_{\rm h}\cdot\boldsymbol{\chi}_{\rm p}(\mathbf{x}, t_{\rm c})\;, \quad \text{and}$$
$$\Upsilon(\mathbf{x}_1,\mathbf{x}_2) = \mathcal{F}(\mathbf{x}_1)\mathcal{F}^*(\mathbf{x}_2)\mathcal{J}(\mathbf{x}_1)\mathcal{J}^*(\mathbf{x}_2)\;.$$

We have here approximated $t_{\rm s} \approx t_{\rm c}(y) =$constant in $\mathbf{k}$.

The averaged product, or spectrum, is now written as:

$$\langle \hat{I}_{\rm c}(\mathbf{k})\hat{I}^*_{\rm c}(\mathbf{k})\rangle = \iint d\mathbf{x}_1 d\mathbf{x}_2\, \langle e^{-i(2\mathbf{k}_{\rm h}\cdot(\mathbf{x}_1-\mathbf{x}_2)+\zeta(\mathbf{x}_1)-\zeta(\mathbf{x}_2))}\Upsilon(\mathbf{x}_1,\mathbf{x}_2) \, \tilde{U}(x'_{\rm s})\tilde{U}(x'_{\rm s})\tilde{V}(y_{\rm s}(\mathbf{x}_1))\tilde{V}(y_{\rm s}(\mathbf{x}_2))\rangle\;, \tag{14}$$

where we have made use of the fact that $\tilde{U}$ and $\tilde{V}$ are real functions.

Estimating the Doppler frequency using the method of moments

Assume for a moment that we have a function h, where $h(k-\tilde{\mu})$ is symmetric around $\tilde{\mu}$. The $n^{\rm th}$ order moment of this function is given by

$$\mathrm{m}_n \equiv \int dk\, k^n h(k-\tilde{\mu}) = \int dk\, (k+\tilde{\mu})^n h(k)\;,$$

and the shift $\tilde{\mu}$ is given by $\tilde{\mu} = \mathrm{m}_1/\mathrm{m}_0$. This technique is known as the method of moments, and we will here use it to estimate the Doppler frequency.

For our function $\langle \hat{I}_{\rm c}(\mathbf{k})\hat{I}^*_{\rm c}(\mathbf{k})\rangle$, the $0^{\rm th}$ and $1^{\rm st}$ order moments are defined as:

$$\mathrm{m}_0 = \int d\mathbf{k}\, \langle \hat{I}_{\rm c}(\mathbf{k})\hat{I}^*_{\rm c}(\mathbf{k})\rangle\;, \tag{15}$$

$$\mathrm{m}_1 = \int d\mathbf{k}\, k_{\rm y} \langle \hat{I}_{\rm c}(\mathbf{k})\hat{I}^*_{\rm c}(\mathbf{k})\rangle\;. \tag{16}$$

In order to calculate the azimuthal shift, we make the following variable transformation:

$$k_{\rm y} = \tilde{k}_{\rm y} - \frac{1}{2v}\left(\dot{\zeta}(\mathbf{x}_1)+\dot{\zeta}(\mathbf{x}_2)\right) \equiv \tilde{k}_{\rm y} - \Sigma\tilde{k}_{\rm y} \tag{17}$$

$$k_{\rm x} = \tilde{k}_{\rm x}\;, \tag{18}$$

and define

$$U(k_{\rm x}) = \tilde{U}\left(-\frac{1}{\alpha}\frac{k_{\rm r}}{k_{\rm h}}k_{\rm x}\right)\;, \quad V(k_{\rm y}) = \tilde{V}\left(-\frac{R}{2k_{\rm r}}k_{\rm y}\right)\;.$$

The $0^{\rm th}$ and $1^{\rm st}$ order moments defined in (15)-(16) are then given by:

$$\mathrm{m}_0 = \iint d\mathbf{x}_1 d\mathbf{x}_2\, \langle\, e^{-i(2\mathbf{k}_{\rm h}\cdot(\mathbf{x}_1-\mathbf{x}_2)+\zeta(\mathbf{x}_1)-\zeta(\mathbf{x}_2))}\Upsilon(\mathbf{x}_1,\mathbf{x}_2) \int d\tilde{\mathbf{k}}\, U(\tilde{k}_{\rm x})^2 V(\tilde{k}_{\rm y}+\Delta\tilde{k}_{\rm y})V(\tilde{k}_{\rm y}-\Delta\tilde{k}_{\rm y})\rangle\;, \tag{19}$$

$$\mathrm{m}_1 = \iint d\mathbf{x}_1 d\mathbf{x}_2\, \langle\, e^{-i(2\mathbf{k}_{\rm h}\cdot(\mathbf{x}_1-\mathbf{x}_2)+\zeta(\mathbf{x}_1)-\zeta(\mathbf{x}_2))}\Upsilon(\mathbf{x}_1,\mathbf{x}_2) \int d\tilde{\mathbf{k}}\, (\tilde{k}_{\rm y}-\Sigma\tilde{k}_{\rm y})U(\tilde{k}_{\rm x})^2 V(\tilde{k}_{\rm y}+\Delta\tilde{k}_{\rm y})V(\tilde{k}_{\rm y}-\Delta\tilde{k}_{\rm y})\rangle, \tag{20}$$

where $\Delta\tilde{k}_{\rm y} \equiv (\dot{\zeta}(\mathbf{x}_1)-\dot{\zeta}(\mathbf{x}_2))/2v$.

It is known that the radar ground-pattern intensity function V is a symmetric function in $\tilde{k}_{\rm y}$, and consequently the product $V(\tilde{k}_{\rm y}+\Delta\tilde{k}_{\rm y})V(\tilde{k}_{\rm y}-\Delta\tilde{k}_{\rm y})$ is symmetric in $\tilde{k}_{\rm y}$. Therefore,

$$\int d\tilde{\mathbf{k}}\, U(\tilde{k}_{\rm x})^2 V(\tilde{k}_{\rm y}+\Delta\tilde{k}_{\rm y})V(\tilde{k}_{\rm y}-\Delta\tilde{k}_{\rm y})\tilde{k}_{\rm y} = 0\;, \tag{21}$$

and we obtain the following expression for m_1:

$$\mathrm{m}_1 = -\iint d\mathbf{x}_1 d\mathbf{x}_2\, \langle\, e^{-i(2\mathbf{k}_{\rm h}\cdot(\mathbf{x}_1-\mathbf{x}_2)+\zeta(\mathbf{x}_1)-\zeta(\mathbf{x}_2))}\Upsilon(\mathbf{x}_1,\mathbf{x}_2) \, \Sigma\tilde{k}_{\rm y}\int d\tilde{\mathbf{k}}\, U(\tilde{k}_{\rm x})^2 V(\tilde{k}_{\rm y}+\Delta\tilde{k}_{\rm y})V(\tilde{k}_{\rm y}-\Delta\tilde{k}_{\rm y})\rangle\;. \tag{22}$$

Note that m_1 only differs from m_0 through the presence of the shift-factor $\Sigma\tilde{k}_{\rm y}(\mathbf{x}_1,\mathbf{x}_2)$.

Because the EM-width is small, the lag between $\mathbf{x}_1$ and $\mathbf{x}_2$ in (19)-(22) is small. Here, $\dot{\boldsymbol{\chi}}_{\rm p}$ is effectively the orbital velocity of the *long* waves, and this will not change much due to small variations in $\mathbf{x}$. Hence, we may neglect the difference $\dot{\zeta}(\mathbf{x}_1)-\dot{\zeta}(\mathbf{x}_2)$ and approximate $V(\tilde{k}_{\rm y}+\Delta\tilde{k}_{\rm y})V(\tilde{k}_{\rm y}-\Delta\tilde{k}_{\rm y}) \approx V(\tilde{k}_{\rm y})^2$, so that the $\tilde{\mathbf{k}}$-integral may be put outside the expectation-operator in equations (19) and (22).

Assuming statistical stationarity with respect to $\mathbf{x}$, the Doppler frequency (in the unit of Hertz) is now given by:

$$\mu = -\frac{1}{4\pi}\frac{\int d\mathbf{x}\, e^{-2i\mathbf{k}_{\mathrm{h}}\cdot\mathbf{x}}\langle\, e^{\Lambda(\mathbf{x})}\Upsilon(\mathbf{x},\mathbf{0})(\dot{\zeta}(\mathbf{x})+\dot{\zeta}(\mathbf{0}))\rangle}{\int d\mathbf{x}\, e^{-2i\mathbf{k}_{\mathrm{h}}\cdot\mathbf{x}}\langle\, e^{\Lambda(\mathbf{x})}\Upsilon(\mathbf{x},\mathbf{0})\rangle} \tag{23}$$

where we have defined $\Lambda(\mathbf{x}) = i(\zeta(\mathbf{0})-\zeta(\mathbf{x}))$.

3. COMPUTATION

In order to compute the theoretical Doppler frequency given in eq. (23), the Fourier kernels $\langle\, e^{\Lambda(\mathbf{x})}\Upsilon(\mathbf{x},\mathbf{0})(\dot{\zeta}(\mathbf{x}) + \dot{\zeta}(\mathbf{0}))\rangle$ and $\langle\, e^{\Lambda(\mathbf{x})}\Upsilon(\mathbf{x},\mathbf{0})\rangle$ need to be computed. To do this, expressions for $\mathcal{F}$ and $\mathcal{J}$ in Υ, and a statistical model for the sea surface represented by ζ, are needed.

3.1. The electromagnetic scattering model

In [5], a scattering model is developed that enables us to calculate $\mathcal{F}(\mathbf{x})$ for a given surface, scattering geometry and global polarization vectors $\hat{\mathbf{H}}_{\mathrm{i}}$ (incident) and $\hat{\mathbf{H}}_{\mathrm{s}}$ (scattered). The model source function $\mathcal{F}(\mathbf{x})$ is here written as a sum

$$\mathcal{F}(\mathbf{x}) = F_0 + F_1(\mathbf{x})\,, \tag{24}$$

where the lower indexes refers to the order of dependence on $(\boldsymbol{\xi},\eta)$.

Explicitly, the 0^{th} order source function is

$$F_0 = \hat{\mathbf{H}}_{\mathrm{s}}\cdot\left\{\mathcal{B}^{(0)}_{vv}\hat{\mathbf{v}}^{(0)}\hat{\mathbf{v}}^{(0)} + \mathcal{B}^{(0)}_{ww}\hat{\mathbf{w}}^{(0)}\hat{\mathbf{w}}^{(0)}\right\}\cdot\hat{\mathbf{H}}_{\mathrm{i}}\,, \tag{25}$$

where $\mathcal{B}^{(0)}_{vv} = \mathcal{B}^{(0)}_{ww} = 2(\nu-1)/(n_z(\nu+1))$ are the Kirchhoff reflection coefficients for specular reflection [7], ν is the complex reflection index between the two media (here air and water), n_z is the z-component of the unit surface normal, and $\hat{\mathbf{v}}^{(0)} = [0,1,0]$, $\hat{\mathbf{w}}^{(0)} = -\hat{\mathbf{k}}_{\mathrm{r}}\times\hat{\mathbf{v}}^{(0)}$ are the local vertical and horizontal magnetic polarization vectors, respectively. F_0 is thus the tangent plane approximation of the source function.

The first order source function describes the effect of first order generalized (surface) curvature on the backscattered signal with no approximation in slope. It may be expressed by an integral over a transfer function,

$$F_1(\mathbf{x}) = \int d\mathbf{k}\, e^{i\mathbf{k}\cdot\mathbf{x}}T_F(\mathbf{k})\,\hat{\eta}(\mathbf{k})\,, \qquad \text{where} \tag{26}$$

$$\begin{aligned} T_F &= 2ik_{\mathrm{v}}F_0 \\ &\quad + \hat{\mathbf{H}}_{\mathrm{s}}\cdot\left\{\mathcal{B}^{(1)}_{vv}\hat{\mathbf{v}}^{(1)}\hat{\mathbf{v}}^{(1)} + \mathcal{B}^{(1)}_{ww}\hat{\mathbf{w}}^{(1)}\hat{\mathbf{w}}^{(1)}\right\}\cdot\hat{\mathbf{H}}_{\mathrm{i}}\,. \end{aligned} \tag{27}$$

Here,

$$\mathcal{B}^{(1)}_{ww} = 4ik_{\mathrm{r}}\frac{(\nu^2-1)\left(\sin^2\theta_i+\cos^2\theta_t\right)}{\left(\nu\cos\theta_i+\cos\theta_t\right)^2}\cos^2\theta_i\,, \tag{28}$$

$$\mathcal{B}^{(1)}_{vv} = 4ik_{\mathrm{r}}\frac{(\nu^2-1)}{\left(\cos\theta_i+\nu\cos\theta_t\right)^2}\cos^2\theta_i \tag{29}$$

are equivalent to the SPM-1 coefficients of Valenzuela [9] computed at the local incident and transmitted angles. Specifically, θ_i is the local incident angle, computed at the slope $\mathbf{s} = (2\mathbf{k}^{\mathrm{i}}_{\mathrm{h}} - \mathbf{k})/2k^{\mathrm{i}}_{\mathrm{z}}$, θ_t is the local transmitted angle, related to θ_i by Snell's law, and $\hat{\mathbf{w}}^{(1)}(\mathbf{k}) = -(\mathbf{k}\times\mathbf{k}_{\mathrm{r}})/|\mathbf{k}\times\mathbf{k}_{\mathrm{r}}|$, $\hat{\mathbf{v}}^{(1)}(\mathbf{k}) = \hat{\mathbf{k}}_{\mathrm{r}}\times\hat{\mathbf{w}}^{(1)}$ are the first order local horizontal and vertical magnetic polarization vectors, respectively. Note that it is this surface curvature dependent term that leads to polarization differences in the backscattered signal.

Finally, the Jacobi determinant $\mathcal{J}$ that occurs in Υ may be approximated by:

$$\mathcal{J}(\mathbf{x}) \approx 1 + \nabla\cdot\boldsymbol{\xi} = 1 + J_1(\mathbf{x})\,.$$

3.2. Statistical expressions

Up to order two in surface elevation, we can now write

$$\Upsilon(\mathbf{x},\mathbf{0}) = f(\mathbf{x})f^*(\mathbf{0})\,, \tag{30}$$

where

$$f(\mathbf{x}) = \underbrace{F_0}_{f_0} + \underbrace{(F_0J_1(\mathbf{x}) + F_1(\mathbf{x}))}_{f_1}\,, \tag{31}$$

and the lower indexes of f again refers to the order of dependence on $(\boldsymbol{\xi},\eta)$. Assuming Gaussian statistics, this now yields:

$$\begin{aligned} \langle e^{\Lambda}\Upsilon\rangle &= e^{\varphi_{\zeta\zeta}(\mathbf{x})-\varphi_{\zeta\zeta}(\mathbf{0})} \\ &\quad \Big\{\varphi_{f_1f_1}(\mathbf{x}) + \Big(f_0 + i\left(\varphi_{f_1\zeta}(\mathbf{x}) - \varphi_{f_1\zeta}(\mathbf{0})\right)\Big) \\ &\quad \Big(f_0^* - i\left(\varphi_{\zeta f_1}(\mathbf{x}) - \varphi_{\zeta f_1}(\mathbf{0})\right)\Big)\Big\} \end{aligned} \tag{32}$$

and

$$
\begin{aligned}
&\langle e^{\Lambda}\Upsilon(\dot{\zeta}(\mathbf{x})+\dot{\zeta}(\mathbf{0}))\rangle = e^{\varphi_{\zeta\zeta}(\mathbf{x})-\varphi_{\zeta\zeta}(\mathbf{0})} \\
&\Big\{ if_0\varphi_{\dot{\zeta}\zeta}(\mathbf{x})\Big(f_0^* - i\left(\varphi_{\zeta f_1}(\mathbf{x})-\varphi_{\zeta f_1}(\mathbf{0})\right)\Big) \\
&\quad - if_0^*\varphi_{\zeta\dot{\zeta}}(\mathbf{x})\Big(f_0 + i\left(\varphi_{f_1\zeta}(\mathbf{x})-\varphi_{f_1\zeta}(\mathbf{0})\right)\Big) \\
&\quad - f_0\varphi_{\dot{\zeta}\zeta}(\mathbf{x})\Big(\varphi_{\zeta f_1}(\mathbf{x})-\varphi_{\zeta f_1}(\mathbf{0})\Big) \\
&\quad - f_0^*\varphi_{\dot{\zeta}\zeta}(\mathbf{x})\Big(\varphi_{f_1\zeta}(\mathbf{x})-\varphi_{f_1\zeta}(\mathbf{0})\Big) \\
&\quad + f_0^*\left(\varphi_{f_1\dot{\zeta}}(\mathbf{x})+\varphi_{f_1\dot{\zeta}}(\mathbf{0})\right) \\
&\quad + f_0\left(\varphi_{\dot{\zeta}f_1}(\mathbf{x})+\varphi_{\dot{\zeta}f_1}(\mathbf{0})\right) \\
&\quad - i\left(\varphi_{f_1\dot{\zeta}}(\mathbf{x})+\varphi_{f_1\dot{\zeta}}(\mathbf{0})\right)\left(\varphi_{\zeta f_1}(\mathbf{x})-\varphi_{\zeta f_1}(\mathbf{0})\right) \\
&\quad + i\left(\varphi_{\dot{\zeta}f_1}(\mathbf{x})+\varphi_{\dot{\zeta}f_1}(\mathbf{0})\right)\left(\varphi_{f_1\zeta}(\mathbf{x})-\varphi_{f_1\zeta}(\mathbf{0})\right) \\
&\quad + i\varphi_{f_1f_1}(\mathbf{x})\left(\varphi_{\dot{\zeta}\zeta}(\mathbf{x})-\varphi_{\zeta\dot{\zeta}}(\mathbf{x})\right) \\
&\quad + i\left(\varphi_{\dot{\zeta}\zeta}(\mathbf{x})-\varphi_{\zeta\dot{\zeta}}(\mathbf{x})\right)\left(\varphi_{f_1\zeta}(\mathbf{x})-\varphi_{f_1\zeta}(\mathbf{0})\right) \\
&\qquad \left(\varphi_{\zeta f_1}(\mathbf{x})-\varphi_{\zeta f_1}(\mathbf{0})\right)\Big\} .
\end{aligned}
\tag{33}
$$

Here, it is made use of the fact that $\varphi_{\dot{\zeta}\zeta}(\mathbf{0}) = \varphi_{\zeta\dot{\zeta}}(\mathbf{0}) = 0$. Furthermore, the needed transfer functions are:

$$T_\zeta(\mathbf{k}) = 2i\mathbf{k}_{\mathrm{h}}\cdot\hat{\mathbf{k}} + 2k_{\mathrm{v}} \tag{34}$$

$$T_{f_1}(\mathbf{k}) = -kF_0 + T_F \tag{35}$$

$$T_{\dot{\zeta}}(\mathbf{k}) = -i\,(gk)^{1/2}\,T_\zeta(\mathbf{k})\,, \tag{36}$$

and the source terms F_0 and F_1 are given in the previous subsection.

4. RESULTS

4.1. Predicted Doppler frequencies

As noted in section 2, the Doppler frequency μ of the spectrum $\langle \hat{I}_c(\mathbf{k})\hat{I}_c^*(\mathbf{k})\rangle$ is due to the range direction motion of the coherent backscattering elements on the ocean surface during the integration time. Using the model spectrum of Elfouhaily et al [3] as the input wave-number spectrum $S(\mathbf{k})$ (needed in the computations of the covariances in equations (32), (33)), the Doppler frequency is now estimated for different angles of incidence, wind speeds, wind directions and polarizations.

Figure 1 shows μ plotted as a function of incidence angle for two different wind-speeds (7m/s and 15m/s), both for HH- and VV-polarization (the vertical dotted lines indicate the Envisat range of incidence angles). It is clear that the predicted Doppler frequency varies with incidence angle and increases with increasing wind-speed, and that the two polarizations give different values of the frequency. Here, the wind direction ϕ is taken to be the negative range direction (i.e. wind blowing toward the radar). At an incidence angle of $23°$ and a wind speed of 7 m/s, the VV curve of Figure 1 gives a Doppler frequency value of around 30 Hz, which is in good agreement with the values obtained globally from the ASAR wave mode VV data [1].

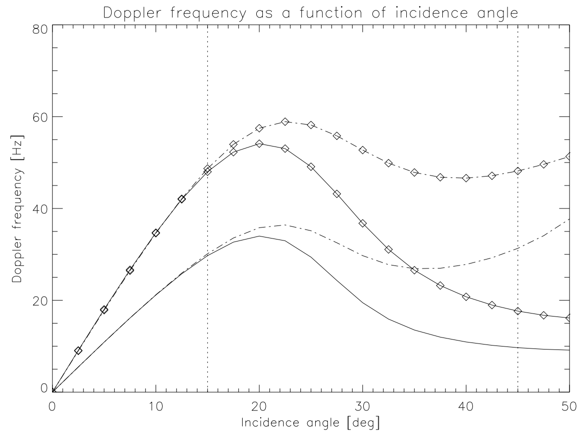

Fig. 1. The Doppler frequency as a function of incidence angle for HH ($-\cdot-$) and VV (—) polarization. Unmarked lines correspond to 7 m/s wind, and lines marked with $\diamond$ to 15 m/s wind.

The motion of the ocean surface can be represented as a wave motion superimposed on a current $\mathbf{U}$. The predicted Doppler frequency may thus be connected to wind waves, surface currents, or a mixture between the two. Here, we are interested in separating the wave motion from the total motion of the surface (i.e. removing $\mathbf{U}$), in order to better estimate the wind. This is achieved by combining the VV and HH Doppler frequencies.

Figure 1 shows that the Doppler frequency μ as a function of incidence angle and wind-speed is different for HH- and VV-polarization. The Doppler frequency due to $\mathbf{U}$ will however be the same for the two polarizations, and so the difference $\mu^{HH} - \mu^{VV}$ will depend on the intrinsic wave velocity, and hence on the wind speed, but not on the surface current. This may be used to estimate the wind speed from the radar image.

From Figure 1 it is clear that the Doppler frequency difference is insignificant for small angles of incidence. In the remaining part of the paper, the incidence angle is fixed at $30°$ (chosen to make the Doppler difference significant).

Sea-state sensitivity, wind direction and wind speed dependency

The idea now is to analyze the Doppler frequency and accompanying frequency difference as functions of wind speed and direction. But first, it is necessary to investigate whether they are more dependent on swell or on shorter wind-waves, in order to assess their abilities to serve as indicators of wind speed.

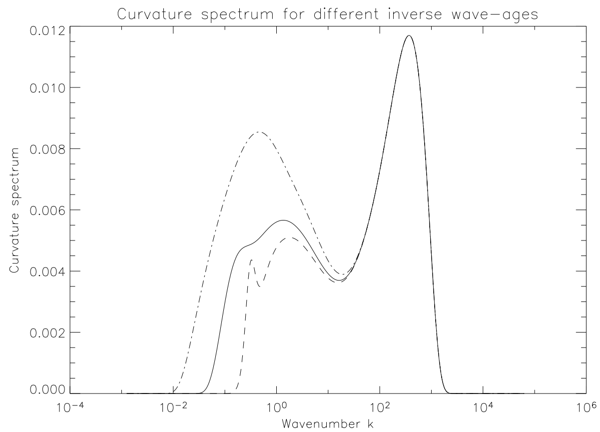

Fig. 2. The curvature spectrum for a wind speed of 7 m/s and different inverse wave ages: — corresponds to $\Omega = 0.84$, $- \cdot -$ to $\Omega = 0.42$, and $--$ to $\Omega = 1.68$.

The curvature spectrum in [3] depends on the dimensionless inverse wave-age parameter Ω, which is equal to 0.84 for fully developed seas. In Figure 2, this spectrum is plotted for 7 m/s wind and $\Omega = \{0.42, 0.84, 1.68\}$. We here observe that decreasing/increasing the value of Ω simply increases/decreases the amount of energy associated with the longest gravity waves (swell), while the short-wave part of the spectrum remains the same. By calculating the Doppler frequency and the frequency difference for different values of Ω, their sea-state dependency may then be investigated.

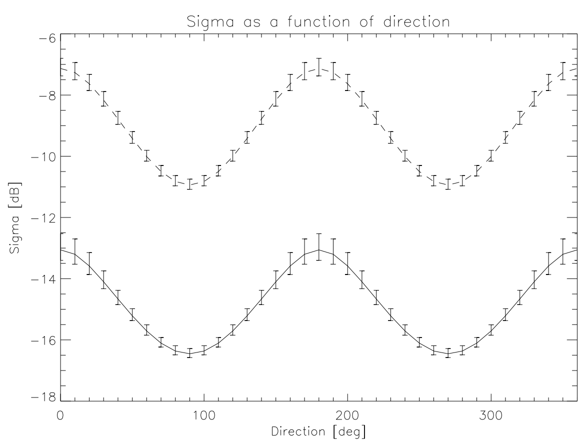

Fig. 3. Sigma (VV) as a function of direction ϕ. Here, the error bounds correspond to an 25% change in inverse wave age Ω. The wind-speed is 7 m/s (—), and 15 m/s $(--)$.

Figures 3- 5 show how the backscatter coefficient σ^{VV} (included for comparison), the Doppler frequency μ^{VV} and the Doppler frequency difference $\mu^{HH} - \mu^{VV}$ all vary as a function of wind direction ϕ, where $\phi = 0°$ is the range direction (i.e. along the radar line of sight). Here, the inverse wave age is $\Omega = 0.84$, and the error bounds correspond to an 25% change in Ω. We observe that both the Doppler frequency and the frequency difference varies periodically as a function of ϕ, with twice the period of σ, and that the variation with inverse wave age is less for the Doppler difference than for the absolute Doppler. Spesifically, the Doppler difference has a maximum relative error of approximately 13%, while the absolute Doppler has a maximum relative error of approximately 25% (15 m/s, $0°$). Therefore, the Doppler frequency difference $\mu^{HH} - \mu^{VV}$ is more suitable for determination of the wind direction.

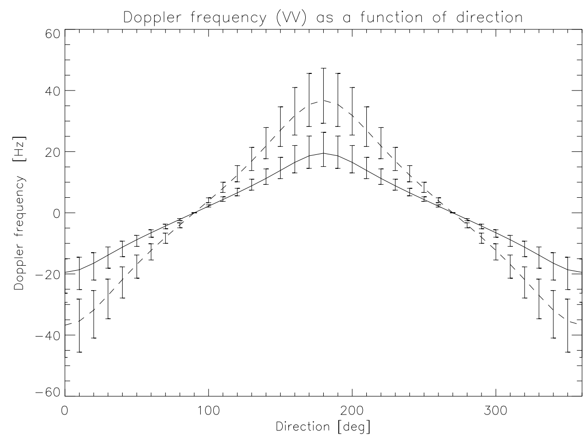

Fig. 4. Doppler frequency (VV) as a function of direction ϕ. Here, the error bounds correspond to an 25% change in inverse wave age Ω. The wind-speed is 7 m/s (—), and 15 m/s $(--)$.

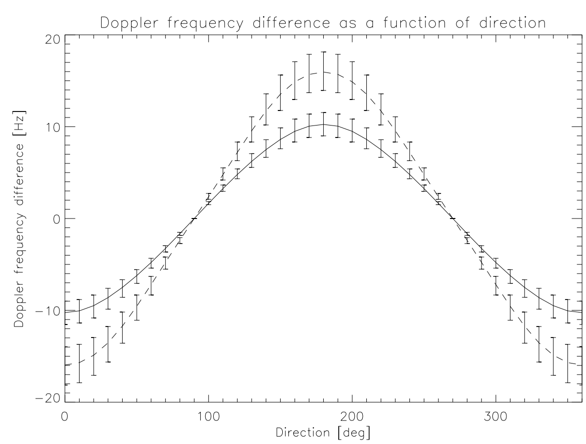

Fig. 5. Doppler frequency difference as a function of direction ϕ. Here, the error bounds correspond to an 25% change in inverse wave age Ω. The wind-speed is 7 m/s (—), and 15 m/s $(--)$.

Estimating the wind speed is also necessary. Figures 6- 7 now shows the Doppler frequency and the frequency difference as functions of wind speed, again for an inverse wave-age of $\Omega = 0.84$ and error bounds corresponding to an 25% change in Ω. First we observe that both the Doppler frequency and the frequency difference increases with increasing wind speed. Also, the variation with Ω is again less for the Doppler difference than for the Doppler itself (with relative errors of approximately 14% vs 25%).

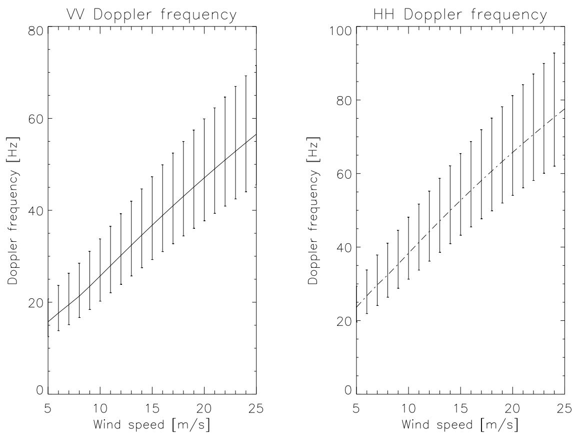

Fig. 6. The Doppler frequency as a function of wind-speed (upwind) for different values of the inverse wave-age and for VV (left) and HH (right) polarization. The angle of incidence is $30°$, and the wind direction is $180°$.

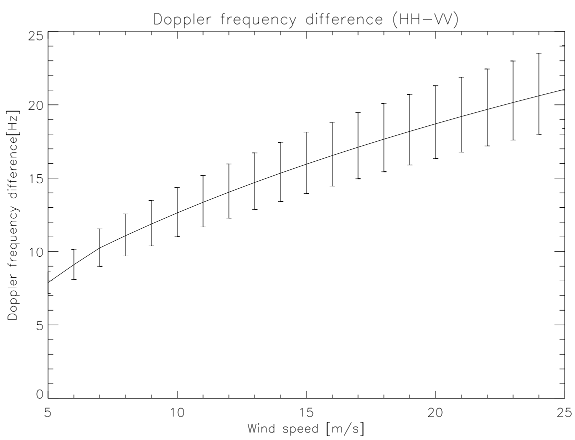

Fig. 7. The Doppler frequency difference $\mu^{HH} - \mu^{VV}$ as a function of wind-speed (upwind) for different values of the inverse wave-age. The angle of incidence is $30°$, and the wind direction is $180°$.

From figures 4-7, we therefore conclude that while the Doppler frequency difference still is sensitive to the sea state, it is less dependent on inverse wave-age than the absolute Doppler frequency is. This implies that the frequency difference is less dependent on swell than the absolute Doppler frequency is, and it is therefore a better indicator on wind-speed and -direction. Nevertheless, the dependency on sea state in the Doppler frequency (and Doppler difference) addresses the need for proper estimation of inverse wave age from SAR data.

The most important reason for using the Doppler difference rather than the absolute Doppler frequency is however that the Doppler frequency due to the surface current, as well as any errors arising from variations in the pointing direction of the instrument, are the same for both polarization channels. Hence, these effects may be eliminated by using the Doppler difference as a measure of surface wave motion.

4.2. Measured Doppler frequencies

In order to compare the theoretically predicted Doppler frequencies with Doppler frequencies measured from Envisat ASAR Alt-Pol data, a SAR scene showing the coast of Denmark (ASA_APC_0PNTSS20031009, taken 09. Oct. 2003, 09:55:16-09:55:58) is selected. The incidence angle is $28.9°$ (IS 3), so a significant Doppler frequency difference is expected. Figure 8 shows the intensity image σ^{HH+VV} for a section of this scene.

The corresponding single-look complex image is processed from the ASAR_APC product using an inhouse processing software. From this SLC-Data, azimuth Fourier spectra are calculated for both polarization channels, and Doppler frequencies are estimated. Figure 9 now shows the Doppler frequencies for VV polarization, with 2 km$\times$ 2 km resolution. Observe that one can easily separate between land and ocean in this figure, and that the largest of the lakes can be identified.

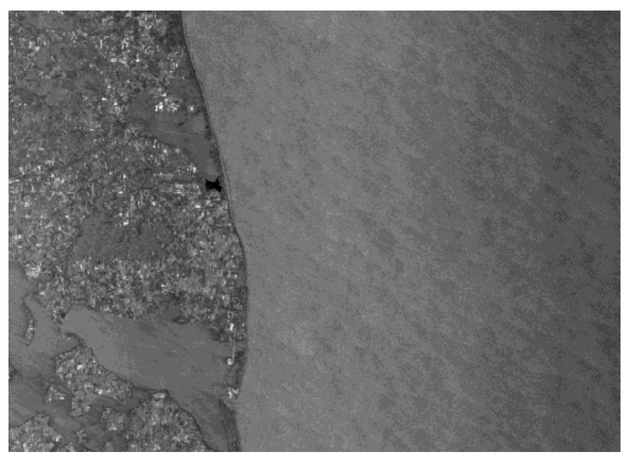

Fig. 8. The intensity image σ^{HH+VV} for a selected SAR scene, showing the coast of Denmark

According to the simulations presented in the previous section, the Doppler frequency difference over ocean is typically in the order of 10 Hz. We are presently not able to measure such a small Doppler difference with 2 km$\times$$2$ km resolution. Figure 10 therefore shows

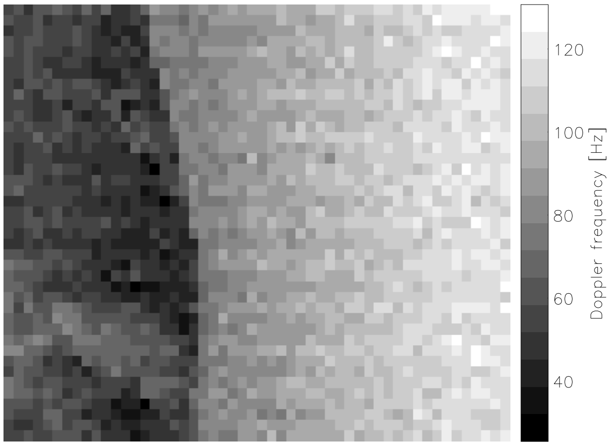

Fig. 9. The Doppler frequency μ^{VV} for a selected SAR scene, showing the coast of Denmark, 2 km$\times$2 km resolution.

$\mu^{HH} - \mu^{VV}$ with 8 km$\times$8 km resolution. Although there is some noise in the image, it is still possible to separate land and ocean in Figure 10.

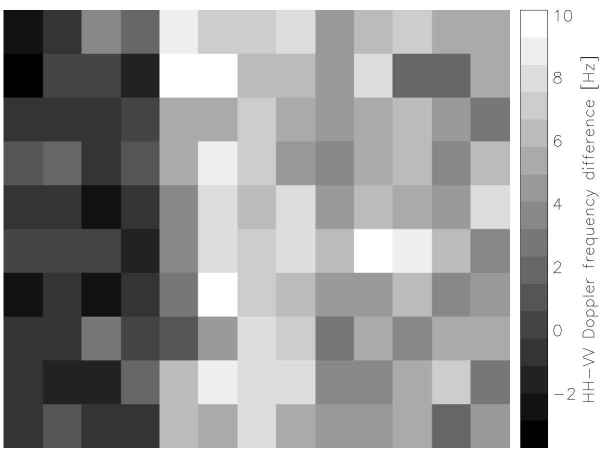

Fig. 10. The Doppler frequency difference $\mu^{HH} - \mu^{VV}$ for a selected SAR scene, showing the coast of Denmark, 8 km$\times$8 km resolution.

Finally, Figure 11 shows an azimuthally averaged profile of the Doppler difference as a function of range. We observe that at the coastline, the Doppler difference abruptly increases with approximately 7 Hz. On the date of these measurements, an oil platform (Sleipner) in the North sea measured a 7.7 m/s wind, with direction (wind coming from) $207°$ measured clockwise from north. According to the simulations above (Fig. 7), a 7 m/s wind in negative range direction will give a Doppler difference of about 10 Hz. Since the wind probably forms an angle with the (negative) range direction, the jump of 7 Hz in the measured Doppler difference is in good agreement with the model predictions.

In Fig. 10, the mismatch between the polarization channels has been compensated for using an average range

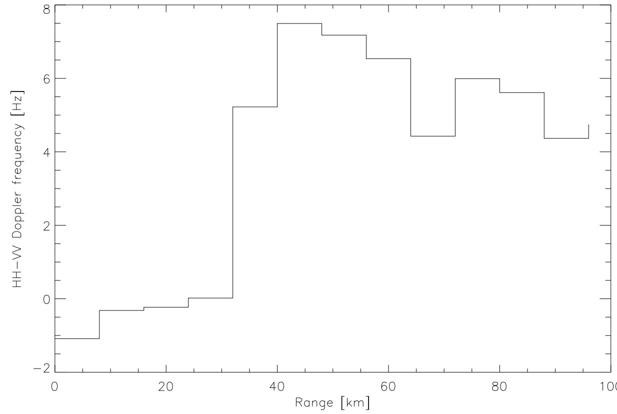

Fig. 11. The (azimuthally averaged) Doppler frequency difference as a function of range.

profile estimated from a pure land scene in the same swath (IS 3).

5. CONCLUSION

The Doppler frequency anomaly in SAR data has recently been shown to be highly correlated to the range direction wind field component. Here, the capabilities of dual polarization SAR data to improve the wind/current retrieval based on Doppler measurements have been investigated.

The theoretical model and simulations presented in this paper shows that the difference between the Doppler frequencies for HH and VV polarization is an even better indicator on wind speed and direction than the Doppler frequency itself is. The reasons for this is that the Doppler difference:

(i) is less dependent on the sea state than the Doppler frequency itself is,

(ii) remove the possible contribution from a steady surface current, and

(iii) remove any errors arising from variations in the pointing direction of the instrument, except effects arising from a mismatch between the polarization channels.

Comparison with Doppler frequency estimates from Envisat ASAR Alt-Pol data show a good agreement between predicted and measured Doppler frequency differences. In the future, it is necessary to establish a large SAR data-set, with co-located wind estimates from platforms, to statistically verify the agreement between Doppler frequency difference and wind conditions. Also, it is clear that to improve the differential Doppler estimates, a method for estimating the inverse wave-age parameter from SAR data is needed. This will be the topic for future work

ACKNOWLEDGMENTS

The work was co-funded by the Research DG of the European Commission under contract EVG1-CT-2001-00051, “EnviWave”, and the Norwegian Research Council under contract 153781/420, “SARA”.

REFERENCES

[1] B. Chapron, F. Collard, and V. Kerbaol. Satellite synthetic aperture radar sea surface doppler measurements, 2003.

[2] M. Van der Kooij, W. Hughes, and S. Sato. Doppler current velocity measurements: A new dimension to spaceborne sar data, available http://atlantisscientific.com/eoserv.html, 2001.

[3] T. Elfouhaily, B. Chapron, K. Katsaros, and D. Vandemark. A unified directional spectrum for long and short wind-driven waves. *J. Geophys. Res.*, 102(C7):15781–15796, July 1997.

[4] G. Engen. *Imaging Ocean Waves with Synthetic Aperture Radar*. PhD thesis, University of Tromsø 1997.

[5] G. Engen, I. F. Pedersen, H. Johnsen, and T. Elfouhaily. Curvature effects in ocean surface scattering, submitted to *IEEE Trans. Antennas. Propag*.

[6] A. Ishimaru. *Electromagnetic wave propagation, radiation, and scattering*. Prentice-Hall International, 1991. ISBN 0-13-273871-6.

[7] A. Ishimaru. *Wave Propagation and Scattering in Random Media*. IEEE Press, 1997. ISBN 0-7803-4717-X.

[8] O. M. Phillips. *The dynamics of the upper ocean*. Cambridge University Press, 1977. ISBN 0-521-21421-1.

[9] G. R. Valenzuela. Depolarization of EM waves by slightly rough surfaces. *IEEE Trans. Antennas Propag.*, 15:552–557, 1967.